ELSEVIER

Contents lists available at ScienceDirect

Applied Catalysis B: Environment and Energy

journal homepage: www.elsevier.com/locate/apcatb



Pseudo-Jahn-Teller effect induced lattice distortion in flexible MOFs boosts electrochemical nitrate reduction reaction

Shuang Zhao ^{a,1}, Jing Wang ^{b,1}, Fangfang Wu ^{c,1}, Xiaoxuan Chen ^a, Fan Wu ^a, Junrong Zou ^a, Haiqiao Zhou ^a, Fenglin Xie ^a, Wei Wang ^a, Peng Gao ^{a,*}, Weiliu Fan ^{d,*}, Wei Ye ^{a,*}

ARTICLE INFO

Keywords: Nitrate reduction reaction Lattice distortion d-band center Pseudo-Jahn-Teller effect Zinc-nitrate battery

ABSTRACT

The green electricity-driven electrocatalytic nitrates to ammonia conversion emerges as an ideal, economical solution for transforming the nitrogen-containing contaminants into valuable chemicals. Herein, we put forward a new lattice distortion strategy in metal-organic frameworks (MOFs) to effectively regulate the d-orbitals electronic structure of the metal nodes to boost ammonia synthesis performance. The longer nickel-oxygen bonds extrude the adjacent cobalt-oxygen bonds in the orderly arranged CoNi dual sites, resulting in the distorted Co-O octahedron. The d-electrons are redistributed, which greatly strengthens the binding of *NHOH intermediate, forming a new energy-efficient rate-determining step in nitrate reduction reaction. Benefitting from the regulated electronic structure, the bimetallic CoNi-MOF nanosheets array electrode delivers a higher ammonia yield rate (1.51 mmol cm $^{-2}$ h $^{-1}$) and Faradaic efficiency (94.1 %) compared to the counterpart Co-MOF and Ni-MOF. Furthermore, the array electrode was assembled into a zinc-nitrate battery, an open-circuit voltage of 1.372 V was achieved, and the maximum output power density reached as high as 8.49 mW cm $^{-2}$.

1. Introduction

Ammonia (NH $_3$) is an essential major chemical product, mainly used as raw material for the manufacture of nitrogen fertilizer, pharmaceuticals, refrigeration, and so on. Besides, ammonia is also regarded as the perfect carbon-free, hydrogen-rich (17.6 wt%) energy medium [1–5]. In industry, ammonia synthesis is proceeded employing the century-old Haber-Bosch method, which is operated at harsh conditions (temperature: 400 $-500\,^{\circ}\text{C}$, pressure: 150 $-300\,$ atm). In order to meet the tremendous demand of ammonia in the global market, ammonia annual output has reached 235 million tons in 2019, this undoubtedly resulted in huge fossil fuel consumption and serious carbon emissions [6]. Electrocatalytic nitrate reduction reaction (NO $_3$ RR) to ammonia is regarded as a strong supplement to the conventional Haber-Bosch process, mainly due to the abundant sources of nitrates, greatly enlarged NH $_3$ yield rate, and higher NH $_3$ Faradaic efficiency (FE) in comparison to

the fascinating electrochemical nitrogen reduction reaction (NRR) [7–17]. Nevertheless, the current electrochemical NO $_3$ RR is still restricted to the low ammonia yield rate and FE toward large-scale industrial application, especially in the low concentration of nitrates.

Nitrates to ammonia conversion ($NO_3^- + 9~H^+ + 8e^- \rightarrow NH_3 + 3~H_2O$) is a multistep coupling process involved nine protons and eight electrons, therefore the complicated N-intermediates are produced on the catalysts surface, and/or the multiple reaction pathways are involved [18,19]. To achieve efficient NO_3RR , the electrocatalysts should possess abundant active sites with tunable electronic structure to meet the requirements of the appropriate adsorption strength for the corresponding N-intermediates, and the declined energy barrier of the rate-determining step (RDS). Lattice distortion, i.e., elongation or compression of the chemical bonds, influences the redistribution of local charges, the spin state of the catalytic centers, and the adsorption configurations of intermediate species, proving to be an effective method to modulate the

^a Key Laboratory of Organosilicon Chemistry and Material Technology, Ministry of Education, Zhejiang Key Laboratory of Organosilicon Material Technology, College of Material, Chemistry and Chemical Engineering, Hangzhou Normal University, Hangzhou, Zhejiang 311121, PR China

b Key Laboratory of Catalytic Conversion and Clean Energy in Universities of Shandong Province, College of Chemistry and Chemical Engineering, Qufu Normal University, Qufu, Shandong 273165, PR China

^c College of Materials Science and Engineering, Zhejiang University of Technology, Hangzhou, Zhejiang 310014, PR China

^d School of Chemistry and Chemical Engineering, Shandong University, Jinan 250100, PR China

^{*} Corresponding authors.

E-mail addresses: gaopeng@hznu.edu.cn (P. Gao), fwl@sdu.edu.cn (W. Fan), yewei@hznu.edu.cn (W. Ye).

 $^{^{1}\,}$ These authors contributed equally to this work.

catalytic performance [20–23]. This lattice distortion is usually caused by the Jahn-Teller effect of metal ions ($\mathrm{Cu^{2+}}$, $\mathrm{Mn^{3+}}$) in octahedral or tetrahedral fields, which leads to the octahedron and tetrahedron to be stretched or compressed, and thus the spin states of central metal ion are split [24,25]. For example, Mn doping can induce the neighboring Ni site to occur Jahn-Teller distortion, leading to the shorted Ni–O bonds, which strengthens orbital hybridization with the p-orbitals of $\mathrm{CO_2}$ and significantly improves $\mathrm{CO_2}$ conversion to CO [26]. Anomalously, lattice distortion has been occurred for metal ions with weak or no Jahn-Teller effect due to the external interactions, which typically attributed to pseudo-Jahn-Teller effect. It is very challenging to precisely modulate lattice distortion to achieve high catalytic activity by pseudo-Jahn-Teller effect, yet very important.

Here, the lattice distortion of the Co-O octahedron was achieved by a pseudo-Jahn-Teller effect of Ni²⁺ doping in bimetallic CoNi-MOF. Due to the flexible ligand environment in MOF, the longer Ni-O bonds extrude the neighboring shorter Co-O bonds, resulting in a stretched Co–O octahedron unit. The electrons in the *d*-orbits were redistributed, up shifting the *d*-band center of Co site. The adsorption strength of the involved N-species was optimized, hence the ΔG value of the potentialdetermination step (PDS) was greatly declined. And thus, the electrochemical NO₃RR performance was boosted. The synthesized CoNi-MOF nanosheets array delivered excellent NH₃ yield rate of 1.51 mmol cm⁻² h⁻¹ and NH₃ FE of 94.1 % at -0.6 V versus reversible hydrogen electrode (RHE), much higher than that of the counterpart Ni-MOF nanorods and Co-MOF nanosheets arrays. Furthermore, CoNi-MOF nanosheets array electrode was assembled into a zinc-nitrate battery, which delivered an open-circuit voltage (OCV) of 1.372 V and the maximum output power density of 8.49 mW cm⁻², demonstrating a bright application prospect.

2. Experiments

2.1. Synthesis of CoNi-MOF nanosheets array

The cleaning of nickel foam (NF) was conducted according to the following procedure: a piece of NF (2.0 ×1.0 cm²) was alternately soaked with hydrochloric acid (1.0 M) and acetone for 30 min to remove the surface oxidation layer and organic residues, respectively. Subsequently, the NF was thoroughly cleaned with pure water and ethanol. After that, the NF was dried in a vacuum oven at 60 °C for 24 h. The CoNi-MOF nanosheets array electrodes were prepared according to the previously reported literature with modification. Nickel acetate tetrahydrate (Ni(CH₃COO)₂·4 H₂O, 0.12 mmol), cobalt nitrate hexahydrate (Co(NO₃)₂·6 H₂O, 0.06, 0.12, 0.18, 0.24 mmol) and benzene-1,4dicarboxylate (BDC, C₈H₆O₄, 0.16 mmol) were dissolved in deionized water (50 mL), the solution was then transferred and sealed in a hydrothermal reactor with polytetrafluoroethylene liner. The reaction was proceeded at 150 °C for 20 h. After it was naturally cooled to room temperature, the electrode was meticulously extracted using tweezers, and thoroughly rinsed several times with water/ethanol until the solution was colorless and transparent. Finally, the electrode was dried in a vacuum oven at 60 °C for 24 h.

2.2. Electrochemical NO₃RR test

The electrochemical experiments were performed in an H-cell with a typical three-electrode system. The CoNi-MOF nanosheets array $(1 \times 1 \text{ cm}^2)$, Ag/AgCl with saturated potassium chloride solution, and Pt plate were used as working electrode, reference electrode and counter electrode, respectively. The cathode and anode chambers were divided by a commercial Nafion 117 membrane. The electrolytes used in cathode and anode chambers were the mixture of KNO₃ (1 M) + KOH (1 M) and KOH solutions (1 M), respectively. The volume of the electrolytes was 30 mL both for cathode and anode, the pH of the electrolyte approached 14. The electrochemical NO₃RR test was triggered by applying a constant potential (-0.1, -0.2, -0.3, -0.4, -0.5, -0.6 V) at the

cathode versus RHE for 1 h. The ammonia generated in the electrolyte was spectroscopically quantified using the Indophenol and Nessler's reagent colorimetric methods. Griess reagent and gas chromatography (GC) were used to quantify the by-product (NO_2^-) and gaseous by-products (H_2, N_2) .

2.3. Theoretical calculation

The spin-polarized DFT calculations of the structural and electronic properties were implemented in the Vienna ab initio simulation package (VASP) [27,28]. The generalized gradient approximation (GGA) realized by Perdew–Burke–Ernzerhof function (PBE) was used to describe the exchange-correlation energy [29,30]. The plane wave cutoff energy was set as 450 eV. The DFT-D3 [31], an empirical dispersion correction, was applied because of its good description of long-range van der Waal's interactions. The Brillouin zone integration was utilized with a $2\times 4\times 1$ k-point grid. The energy and force convergence criteria were set to 10^{-4} eV and 0.02 eV/Å, respectively. To avoid interactions between periodic images, a 20 Å-thick vacuum layer was used in the z-direction.

The reaction free energy difference (ΔG) in the nitrate reduction reaction (NO₃RR) process was calculated according to the computational hydrogen electrode (CHE) model by the following equation [32]:

$$\Delta G = \Delta E + \Delta ZPE - T\Delta S + \int C_p dT$$

where ΔE , ΔZPE , T, ΔS , and C_p are the differences in electronic energy, zero–point energy, temperature (298.15 K), entropy, and heat capacity. The relevant calculation results were obtained by the Vaspkit software [33]. The U_L for NO₃RR can be determined by the following equation:

$$U_L = -\Delta G_{\rm max}/e$$

where ΔG_{max} and e are the maximum change in Gibbs free energy among each step and the elementary charge.

3. Results and discussion

3.1. Synthesis and characterization of the array catalyst

As shown in Fig. 1a, high-quality bimetallic CoNi-MOF nanosheets array was grown on nickel foam using a simple one-step hydrothermal method, in which benzene-1,4-dicarboxylate (BDC) was used as the organic ligands. By adjusting the molar ratios of the Co and Ni precursors (Co:Ni= x), the Co:Ni molar ratios in the final samples were regulated. X-ray diffraction (XRD, Fig. 1b) patterns of the synthesized CoNi-MOF samples indicated that the introduction of Ni doping in Co-MOF to form bimetallic CoNi-MOF did not altered the crystal structure of the original Co-MOF, as the diffraction peaks for all CoNi-MOF samples with x (x = 0.1, 0.5.1, 1.1, 1.5.1 and 2:1) were coincided with that of the Co-MOF (x = 1:0) sample [34]. Furthermore, the presence of the distinctive functional groups of BDC, such as C-O, C-H, C=O, and C=C bonds, were validated by the Fourier transform infrared (FT-IR) spectroscopy, confirming the presence of BDC ligands in MOFs structure (Fig. S1) [35]. Scanning electron microscopy (SEM) characterization was carried out to examine the morphology of the samples (Figs. 1c, 1d, S2). The results indicated that the monometallic Ni-MOF and Co-MOF displayed nanorods array and nanosheets array structure, respectively. With the increasing of Ni doping level, the morphology gradually changed from nanosheets array to nanorods array. When the x = 1:1, the sample still sustained nanosheets structure with the thickness of a single nanosheet around 50 nm (Fig. 1d). Further improving Ni doping amount, the sample fully converted to nanorods array structure. Notably, the electrochemical active area (ECSA) could be increased for bimetallic CoNi-MOF compared with that of Ni-MOF, boosting the final electrochemical performance. High-resolution transmission electron microscopy (HRTEM, Fig. 1e) image showed a lattice spacing of

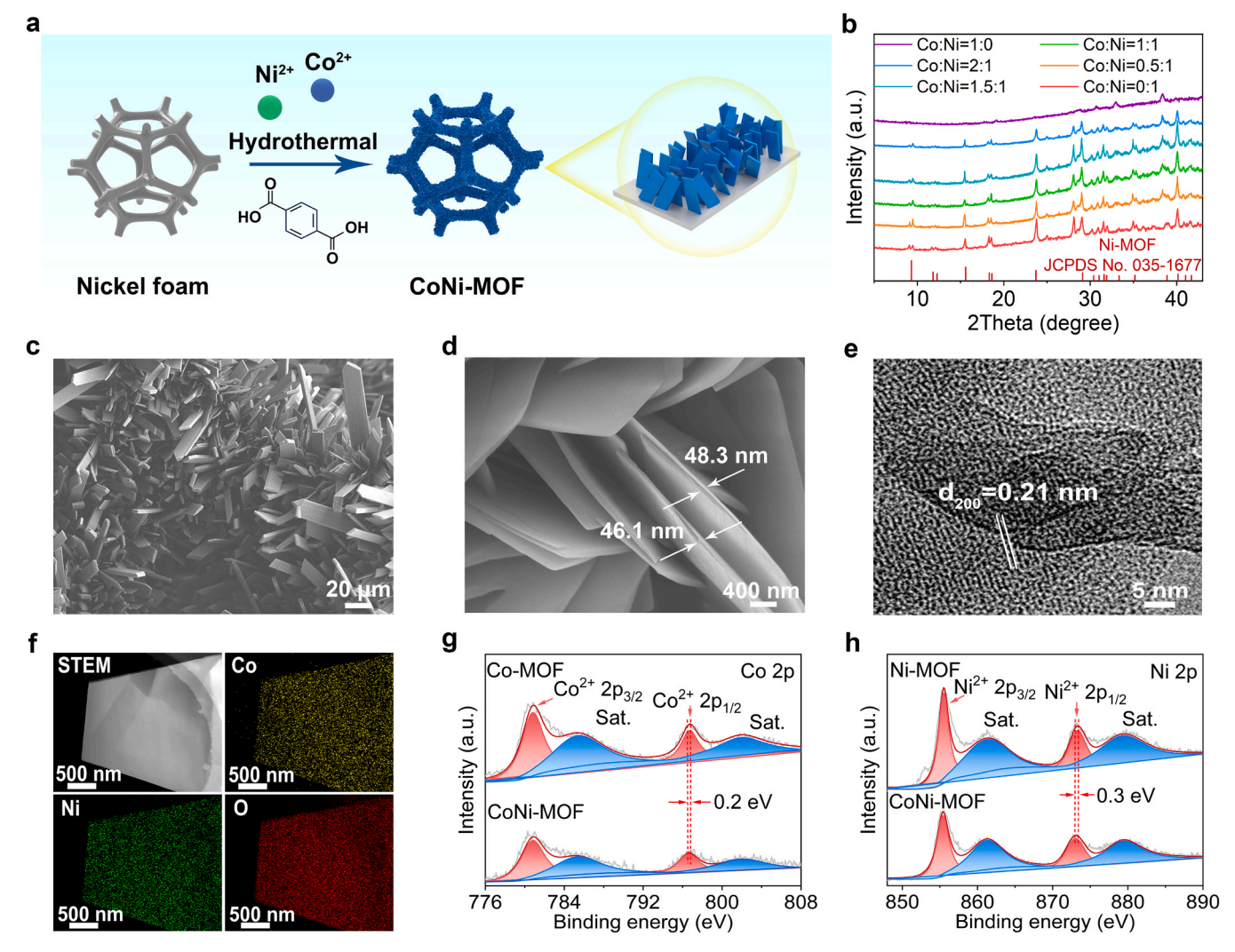


Fig. 1. (a) Schematic demonstration of the one-step hydrothermal synthesis of the bimetallic CoNi-MOF nanosheets array. (b) XRD patterns of CoNi-MOF array samples with different Co:Ni molar ratios. (c, d) SEM images, (e) HRTEM image, and (f) elemental mapping images of CoNi-MOF (x = 1:1) nanosheets array. High-resolution (g) Co 2p and (h) Ni 2p spectra.

0.21 nm, which could be attributed to the (200) plane of CoNi-MOF. As determined by inductively coupled plasma-atomic emission spectroscopy (ICP-AES), the molar ratio of Co:Ni for CoNi-MOF (x=1:1) was 1.06:1, closing to the theoretical value. Elemental mapping images (Fig. 1f) of the single CoNi-MOF nanosheet confirmed the uniform distribution of Co, Ni and O elements across the entire nanosheet, demonstrating the successful formation of bimetallic CoNi-MOF.

X-ray photoelectron spectroscopy (XPS) analysis (Fig. S3) was carried out to reveal the valence state of the Co. Ni elements. A pair of peaks with binding energy located at 780.9 and 796.6 eV were assigned to the $2p_{3/2}$ and $2p_{1/2}$ orbitals of $\text{Co}^{2+},$ respectively. Another pair of peaks with binding energy at 785.8 and 802.0 eV were attributed to the satellite peaks of Co²⁺ 2p (Fig. 1g) [36]. Similarly, the Ni 2p spectrum showed the $2p_{3/2}$ and $2p_{1/2}$ peaks of Ni²⁺ with binding energy at 855.4 eV and 873.0 eV, respectively (Fig. 1h). The satellite peaks of $2p_{3/2}$ and $2p_{1/2}$ of Ni²⁺ were displayed at 861.4 eV and 879.5 eV [37]. In accordance with the structural properties of MOF, the XPS results verified the metal nodes in the bimetallic CoNi-MOF were Co²⁺ and Ni²⁺. It should be noted that the binding energy of Co 2p and Ni 2p for CoNi-MOF was all negatively moved 0.2 eV and 0.3 eV compared with Co-MOF and Ni-MOF, respectively. The results indicated that Ni doping in Co-MOF altered the electronic structure of Co nodes. Furthermore, the bimetallic CoNi-MOF array sample showed good thermal stability, as evidenced by the thermogravimetric (TG) analysis in air, the decomposition temperature of the bimetallic CoNi-MOF was as high as 400 $^{\circ}$ C (Fig. S4).

3.2. Fine structure spectrum characterization of the catalyst

The precise coordination structure of Co and Ni nodes in the bimetallic CoNi-MOF sample was resolved using X-ray absorption fine structure (XAFS) spectrum analysis (Fig. 2). Figs. 2a and 2b showed the Co K-edge X-ray absorption near edge structure spectra (XANES) in reference with Co foil, CoO and Co₃O₄, and Ni K-edge XANES in reference with Ni foil and NiO, respectively. Specifically, the pre-edge for Co K-edge of the CoNi-MOF sample between 7700 and 7720 eV was located between CoO and Co₃O₄, and closer to CoO, suggesting the valence state of $\text{Co}^{\delta+}$ was lower than + 3 and closer to + 2. Moreover, the pre-edge for Ni K-edge of the CoNi-MOF between 8330 and 8350 eV was lower than that of NiO, manifesting the valence state of Ni $^{8+}$ was slightly larger than + 2 in the sample, the valence state of Co and Ni elements coincided with that of the XPS results [38]. Figs. 2c and 2d showed the extended X-ray absorption fine structure spectra (EXAFS) of Co K-edge and Ni K-edge, respectively. Only Co-O bonds were resolved, while Co-Co bonds were absent. Notably, two kinds of Co-O bonds were observed, i. e., tetra-coordinated Co-O bonds with bond length (R) of 1.98 Å, and

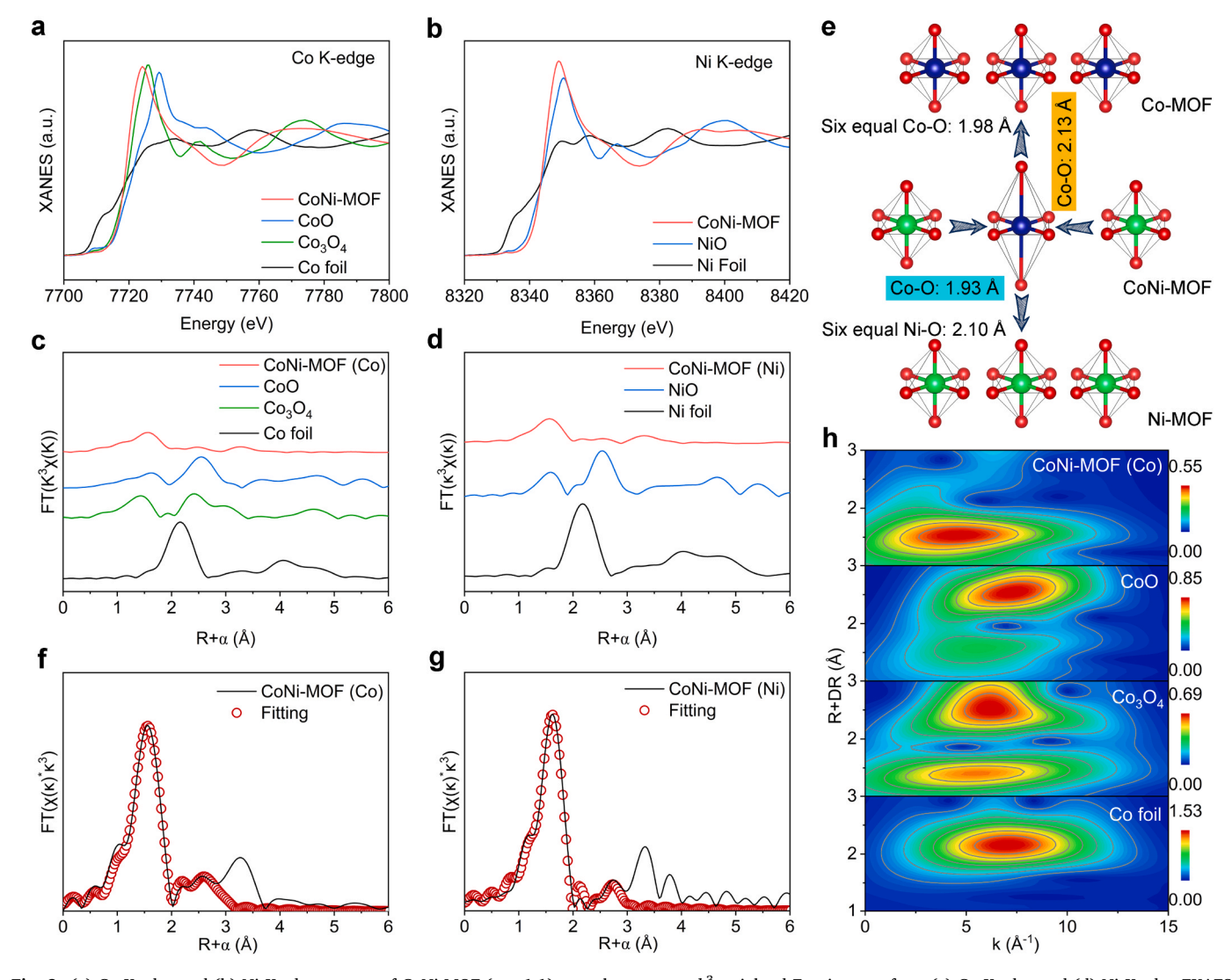


Fig. 2. (a) Co K-edge and (b) Ni K-edge spectra of CoNi-MOF (x = 1:1) nanosheets array. k^3 -weighted Fourier-transform (c) Co K-edge and (d) Ni K-edge EXAFS spectra. (e) Schematic illustration of the lattice distortion of Co–O octahedron of CoNi-MOF in comparison with Co-MOF and Ni-MOF. (f) Co K-edge EXAFS (black line) and (g) Ni K-edge EXAFS spectra and the fitting curves (red circle) of CoNi-MOF array. (h) Wavelet transforms of the k^2 -weighted Co K-edge EXAFS signal for the high-coordination shells.

two-coordinated Co-O bonds with R of 2.08 Å (Table S1). The result indicated that Co²⁺ was coordinated with six oxygen atoms in a distorted octahedral coordination structure. Consistent with the Co case, Ni K-edge EXAFS spectra also resolved two kinds of Ni-O bonds, tetra-coordinated Ni-O bonds with R of 1.82 Å, and two-coordinated Ni-O bonds with R of 2.06 Å, confirming the six-coordinated Ni-O bonds with two kinds of coordination structure in the sample. As predicted by the theoretical calculation and XAFS results (Fig. S5), the monometallic Co-MOF and Ni-MOF delivered conventional octahedral coordination structure with six equal Co-O or Ni-O bonds [39,40]. The distortion of Co-O bonds in bimetallic CoNi-MOF was the result of the different Co-O (1.98 Å) and Ni-O (2.10 Å) bond length (Figs. 2e and S6). In the flexible MOF lattice, the longer Ni-O bonds squeeze the adjacent Co-O bonds located in x-y plane, and thus the Co-O bonds located in z-axis are elongated, forming the distorted Co-O octahedron. Interestingly, the different bond lengths of Co-O and Ni-O bonds were fully consistent with the results predicted by the theoretical calculations in which Co and Ni nodes were orderly arranged (see the details in Fig. S7). This implies that all Co–O octahedrons in CoNi-MOF (x = 1:1) are distorted, and the electronic structure of Co site could be fully regulated (Fig. S8). To further confirm the proposed coordination structure of Co and Ni elements, we also fitted the EXAFS of Co and Ni K-edge based on the octahedral coordinated Ni–O and Co–O structures, and compared with the experimental results of R and K space (Fig. S9). As shown in Figs. 2f and 2g, the fitting curves of Co and Ni EXAFS were almost overlapped with the experimental data, verifying the accuracy of the fine structure. Furthermore, wavelet transform (WT) analysis was performed to further support the above findings. As shown in Fig. 2 h and S10, only Co–O and Ni–O signal was observed for the bimetallic CoNi-MOF sample, while Co–Co and Ni–Ni bonds were absent. Putting together the above results, we came to the conclusion that the bimetallic CoNi-MOF was formed with lattice distortion of Co–O and Ni–O octahedrons.

3.3. Evaluation of catalytic performance

The electrochemical NO₃RR performance of the CoNi-MOF nanosheets array electrodes was assessed in an H-type cell using a standard three-electrode system at room temperature. Firstly, linear scanning voltammetry (LSV) tests were carried out to evaluate the current response. As shown in Fig. 3a, in the mixture solution of KOH and KNO₃, Ni-MOF possessed higher onset potential, but lower current response in

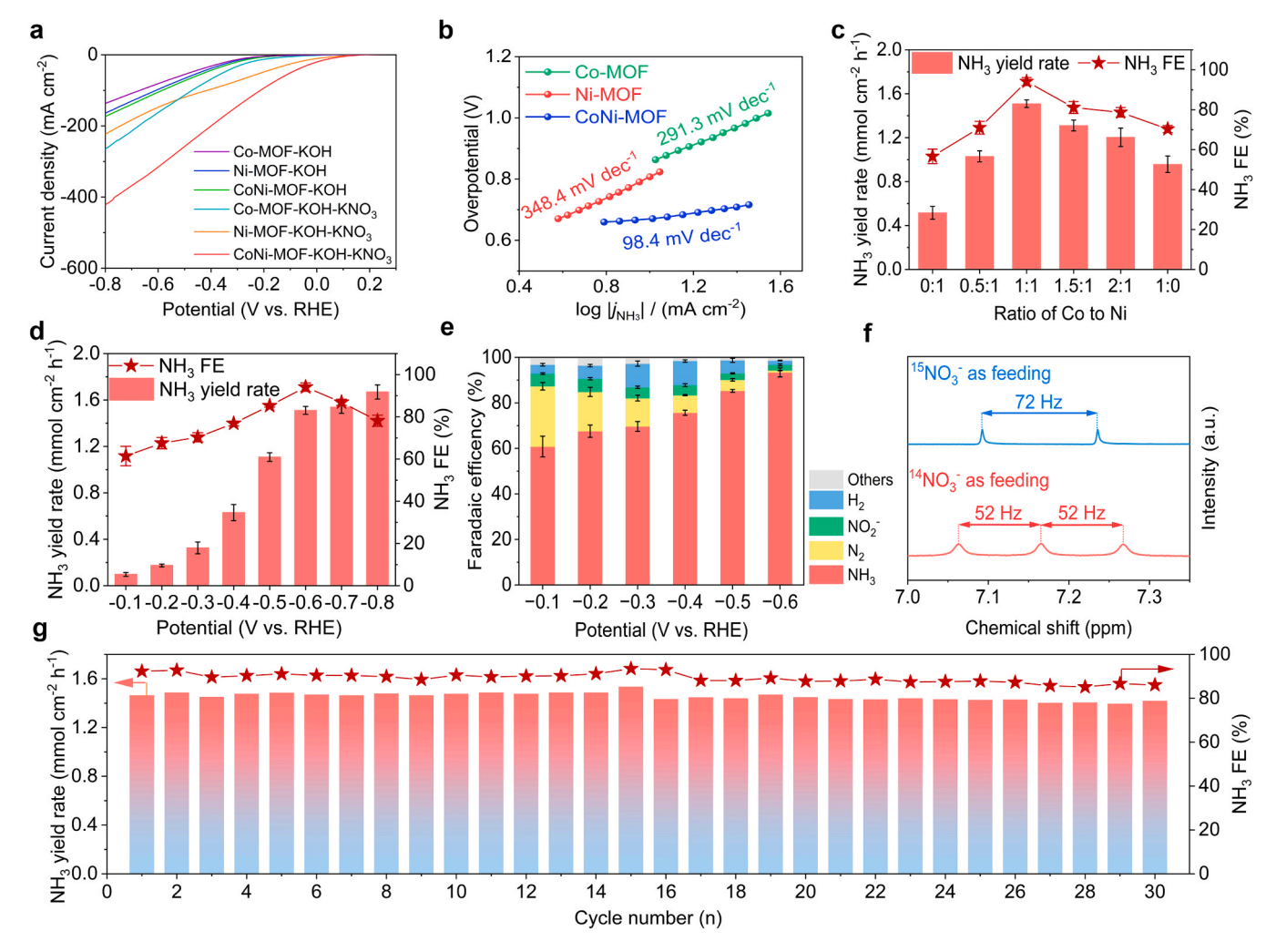


Fig. 3. (a) LSV curves of CoNi-MOF, Ni-MOF, and Co-MOF array in NO₃RR. (b) The Tafel slopes. (c) The relationship of the electrochemical performance for CoNi-MOF array in NO₃RR with different Co:Ni molar ratios. Potential-dependent (d) NH₃ yield rates and (e) the FEs of the possible products for CoNi-MOF (x = 1:1) nanosheet array in NO₃RR. (f) ¹H NMR spectra of the electrolytes using K¹⁴NO₃ and K¹⁵NO₃ as N-source. (g) Cycling stability tests.

the more negative potential region between -0.5 V and -0.8 V versus RHE compared with that of Co-MOF. This implies that the Ni sites in MOFs can more easily trigger the NO₃RR, while Co sites in MOFs improve the kinetics of NO₃RR. It is reasonable to speculate that the bimetallic CoNi-MOF synchronously delivers higher onset potential and larger current density in the low potential range by integrating CoNi dual sites. As expected, the onset potential of CoNi-MOF (x = 1:1) sample positively moved from -0.14 V (Co-MOF) and 0.05 V (Ni-MOF) to 0.14 V. In addition, the current density of the CoNi-MOF nanosheets array was significantly higher than that of the Ni-MOF nanorods and Co-MOF nanosheets array. The above results indicate that the synergistic effect of CoNi dual sites really boosted NO₃RR performance compared with the monometallic Ni-MOF and Co-MOF array. To further investigate the impact of the synergistic effect of CoNi dual sites on the kinetics in NO₃RR, the associated Tafel slopes were obtained (Fig. 3b). Considering the low NH₃ FE (<70 %) within the potential range of Tafel conversion, the NH₃ partial current density (j_{NH3}) was employed to replace the total current density. CoNi-MOF nanosheets array delivered a Tafel slope of 98.4 mV dec⁻¹, much lower than that of Co-MOF (291.3 mV dec⁻¹) and Ni-MOF (348.4 mV dec⁻¹), manifesting the faster NO₃RR conversion kinetics of CoNi-MOF [41].

To screen the optimal molar ratios of Co:Ni in the sample, the NO_3RR performance of the CoNi-MOF samples with varied x was examined at -0.6 V (Figs. 3c and S11). The NH_3 generation rates and NH_3 FEs showed a volcano plot relationship with Co:Ni molar ratios. Notably, CoNi-MOF

(x = 1:1) sample delivered the best NO₃RR performance with NH₃ yield rate of 1.51 mmol cm⁻² h⁻¹ and NH₃ FE of 94.1 %, respectively. The NH₃ yield rate was about 3.0- and 1.6-fold that of Ni-MOF (x = 0.1, $0.51 \text{ mmol cm}^{-2} \text{ h}^{-1}$, 56.6 %) and Co-MOF ($x = 1.0, 0.95 \text{ mmol cm}^{-2}$ h⁻¹, 70.3 %). Hence, unless otherwise emphasized, CoNi-MOF refers to the CoNi-MOF nanosheets array with x = 1:1 in the following text. Upon confirmation the optimal Co:Ni ratio, we further assessed the potentialdependent NO₃RR performance (Fig. S12). As shown in Fig. 3d, the NH₃ yield rates and NH3 FEs greatly increased as the applied potential negatively shifted from -0.1 V to -0.6 V. However, further decreasing the applied potential to -0.7 and -0.8 V, the NH₃ yield rates were further improved, while the NH_3 FEs declined. Notably, CoNi-MOF nanosheets array catalyst exceeds the current state-of-the-art MOF-based electrocatalysts as summarized in Table S2. As NO₃RR is a reduction process involving nine protons and eight electrons, therefore, abundant byproducts could be produced [42]. As such, the FEs of the possible by-products (NO₂, N₂, and H₂) in the NO₃RR were determined (Figs. S13 and S14). As shown in Fig. 3e, the main by-product, N2 displayed a highest FE of 28.6 % at -0.1 V, which quickly dropped to 0.8 % as the potential moved to -0.6 V. Moreover, the NO₂ FE was less than 5 % in the entire potential range, suggesting the effective inhibition of NO₂ for CoNi-MOF. That is because Co element could facilitate NO2-to-NH3 conversion [43]. Notably, H2 FE slightly increased to 10.5 % as the potential moved to -0.3 V, and then decreased to 1.9 % at -0.6 V. In the more negative region, the water splitting process produced more active hydrogen (*H) atoms, which was consumed by the adjacent N-intermediates. Hence, higher NH3 yield rates and lower H2 FE were simultaneously obtained. Obviously, the abundant Co-O6 and Ni-O6 sites and/or the synergistic effect contributed the trade off the NH3 activity and FE. Besides, the ECSA and electrical conductivity also determined the final electrochemical performance. CoNi-MOF nanosheets array displayed a double layer capacitance ($C_{\rm dl}$) of 8.89 mF cm⁻², higher than that of Ni-MOF (3.03 mF cm⁻²) and Co-MOF (6.61 mF cm⁻²) according to the results of the cyclic voltammetry tests (Fig. S15). The results indicated that Co doping in Ni-MOF resulted in the decreased thickness of nanosheets, which really contributed to the larger ECSA and higher performance. Then, electrochemical impedance spectroscopy (EIS) tests were also carried out, the CoNi-MOF nanosheets array delivered a smaller charge transfer resistance than that of Ni-MOF and Co-MOF samples, manifesting the higher electric conductivity of CoNi-MOF (Fig. S16).

To confirm the source of ammonia, nitrogen isotope labelling tests were performed. Hydrogen nuclear magnetic resonance (1 H NMR) spectrum in Fig. 3f showed a triplet peaks with coupling constant of 52 Hz when using $K^{14}NO_3$ as N-feeding, a typical signal of $^{14}NH_4^+$. In contrast, only a double peak with coupling constant of 72 Hz was observed using $K^{15}NO_3$ as N-source, confirming the produced NH $_3$ was really rooted from NO $_3$ RR [44]. In addition, we also assessed the performance of NO $_3$ RR at different concentrations of NO $_3$ and pH. The results indicated that the CoNi-MOF nanosheets array electrode performed well under a wide range of nitrate concentrations and pH conditions (Fig. S17) [45].

The cycling stability is an important parameter in catalyst evaluation. Generally, MOF-based catalysts display poor cycling stability in electrocatalysis that is because the metallic ions nodes could be reduced especially in the low potential range, which is the main obstacle preventing the MOF-based catalysts from achieving large-scale commercial applications [46]. We then assessed the cycling stability of the CoNi-MOF nanosheets array at -0.6 V by repeated NO₃RR cycles (Fig. 3g). Surprisingly, CoNi-MOF electrode could operate stably for continuous thirty cycles (30 h), in which the NH3 yield rates and NH3 FEs were constant without obvious decay, demonstrating the excellent cycling stability of the CoNi-MOF. Then, SEM, XRD and XPS measurement were carried out to inspect the structure stability. SEM images of the CoNi-MOF (Fig. S18) after durability test indicated that the nanosheets array structure was well maintained despite the fact that some nanosheets were slightly bent. XPS results and XRD patterns revealed that the valence state of Co and Ni elements, and phase structure were also sustained, respectively, verifying the metallic ions nodes were not reduced in the long-term cycling test (Figs. S19, S20).

3.4. Study of reaction mechanism

In situ spectroscopic characterizations were employed to clarify the NO₃RR pathway, aiming to deeply investigate the reaction mechanism of the bimetallic CoNi-MOF in NO₃RR. The potential-dependent in situ Raman spectra were firstly acquired to capture the key N-intermediates (Fig. S21). Figs. 4a and S22 showed the in situ Raman spectra between the open circuit potential (OCP) and -0.6 V, the symmetric stretching vibration and N-O bending mode of NO₃ located at 1047 cm⁻¹ and 858 cm⁻¹ emerged starting from OCP [47]. The results indicated that NO₃ was spontaneously adsorbed on the catalyst surface due to the strong interaction of Co node and NO_3^- [48]. The N=O stretching mode of *NO₂ located at 1135 and 1418 cm⁻¹ arose at 0 V, and the intensity gradually increased as the applied potential negatively shifted to -0.6 V [49]. Two possible facts could be speculated from the variation trend of *NO₂ signal: 1. the conversion of NO₃-to-NO₂ could be easily occurred at more positive potential. 2. The accumulation of *NO2 on the catalyst surface suggests the rate-determining step in NO₃RR may root from NO₂-to-NH₃ conversion process. Then, *NOH signal at 1560 cm⁻¹ arose at -0.3 V, indicating that *NO2 undergone further conversion to *NOH

at larger overpotential [50]. The emergence of *NH $_2$ and N–H vibrations located at 1314 cm $^{-1}$ and 1517 cm $^{-1}$ confirmed the formation of NH $_3$ [51,52]. The aforementioned Raman spectroscopic result confirmed some key N-intermediates in NO $_3$ RR, however, it was still not sufficient to infer the whole reaction pathway. Then, in situ differential electrochemical mass spectrometry (DEMS) measurement was performed to capture the missing intermediates (Fig. S23). As shown in Fig. 4b, NO, NOH, NHOH, NH $_2$ OH, NH $_2$ and NH $_3$ species were detected. According to the in situ Raman and DEMS results, the specific pathway of NO $_3$ RR was clarified and displayed in Fig. S24.

Upon confirmation the reaction pathway, density functional theory (DFT) calculations were carried out to deeply understand the reaction mechanism from the viewpoint of energy. Since both Ni-MOF and Co-MOF samples have displayed distinct NO₃RR activities, and thus Ni-O and Co-O sites in Ni-MOF and Co-MOF could serve as active sites for NO₃RR [53,54]. Although Co and Ni atoms were uniformly distributed in the bimetallic MOF, the specific arrangement of Co and Ni nodes could greatly determine the final NO₃RR performance [39]. In our case, theoretical calculation was further employed to screen the most stable structure. The results indicated that the Co and Ni atoms preferred to be individually arranged in an orderly linear sequence, similar with that of intermetallic compound, and the configuration was the most stable, consistent with EXAFS results (Fig. S25). Then, differential charge analysis was carried out to inspect the electronic structure on distorted Co site (Fig. 4c). The Co site with lattice distortion transferred 1.30 e⁻ to the ligands though Co-O bonds, lower than that (1.33 e-) with the conventional Co-O octahedron (Co-MOF, Fig. S26), suggesting more d-orbital electrons, consistent with the XPS result (Figs. 1g, 1h). Accordingly, the d-band center (ε_d , eV) of CoNi-MOF(Co site) moved upward from -1.29 eV (Co-MOF) to -1.22 eV, while the d-band center of CoNi-MOF(Ni site) moved down from -1.58 eV (Ni-MOF) to -1.90 eV (Figs. 4d and S27). This suggests that the Co site could have stronger interaction with the N-intermediates in NO₃RR, which would improve the catalytic activity (Fig. S28) [55]. The distorted Co-O octahedron forced the splitting of the d-orbitals, which resulted in the up-shifted d-band center (Fig. S29) [56]. To demonstrate the universality of the lattice distortion in regulating the electronic structure, we also screened other bimetallic CoM-MOFs (M= Mn, Cu, Zn). As shown in Fig. S30, the d-band center and the average Co-O bond length display a volcano plot trend, suggesting the lattice distortion is a universal strategy in regulating the electronic structure. Furthermore, this trend was also verified by the NO₃RR performance of the bimetallic CoM-MOFs. Then, the limiting potentials of NO₃RR at the above four sites were further calculated in an attempt to validate the aforementioned conjecture. CoNi-MOF(Co site) delivered a lower absolute value of the limiting potential than that of the CoNi-MOF(Ni site), suggesting that the Co site in CoNi-MOF was the real active site for NO₃RR (Fig. S31).

The free energy change (ΔG) in NO₃RR at each site was further calculated following the above reaction pathway (Fig. S24). Fig. 4e showed the energy profiles of NO₃RR, and the corresponding N-intermediates adsorption configurations at the CoNi-MOF(Co site). NO₃ ions preferred to adsorb at the Co site of CoNi-MOF, which was confirmed by the larger adsorption energy than that at Ni site (Fig. S32). Then, *NO₃ undergone multistep spontaneous hydrogenation and dehydration processes to *NO (*NO₃ \rightarrow *NO₂ \rightarrow *NO₂H \rightarrow *NO). Subsequently, the conversion of *NO-to-*NOH process was endothermic with a ΔG_{max} value of 0.14 eV, which was also regarded as the PDS. After that, *NOH was converted to NH3 through a series of exothermic processes. Notably, the reaction pathways were the same with regard to CoNi-MOF(Ni site), Ni-MOF, and Co-MOF (Figs. S33-S35, Table S3). The PDS for CoNi-MOF(Ni site) was *NO \rightarrow *NOH with a $\Delta G_{\rm max}$ value of 0.55 eV, much larger than that at Co site of CoNi-MOF. In contrast, the PDS of Ni-MOF and Co-MOF were *NO→*NOH and *NOH→NHOH, respectively, with $\Delta G_{\rm max}$ values of 0.38 eV and 0.36 eV, respectively, all larger than that of CoNi-MOF (Co site), which well explains the higher NO₃RR performance of CoNi-MOF.

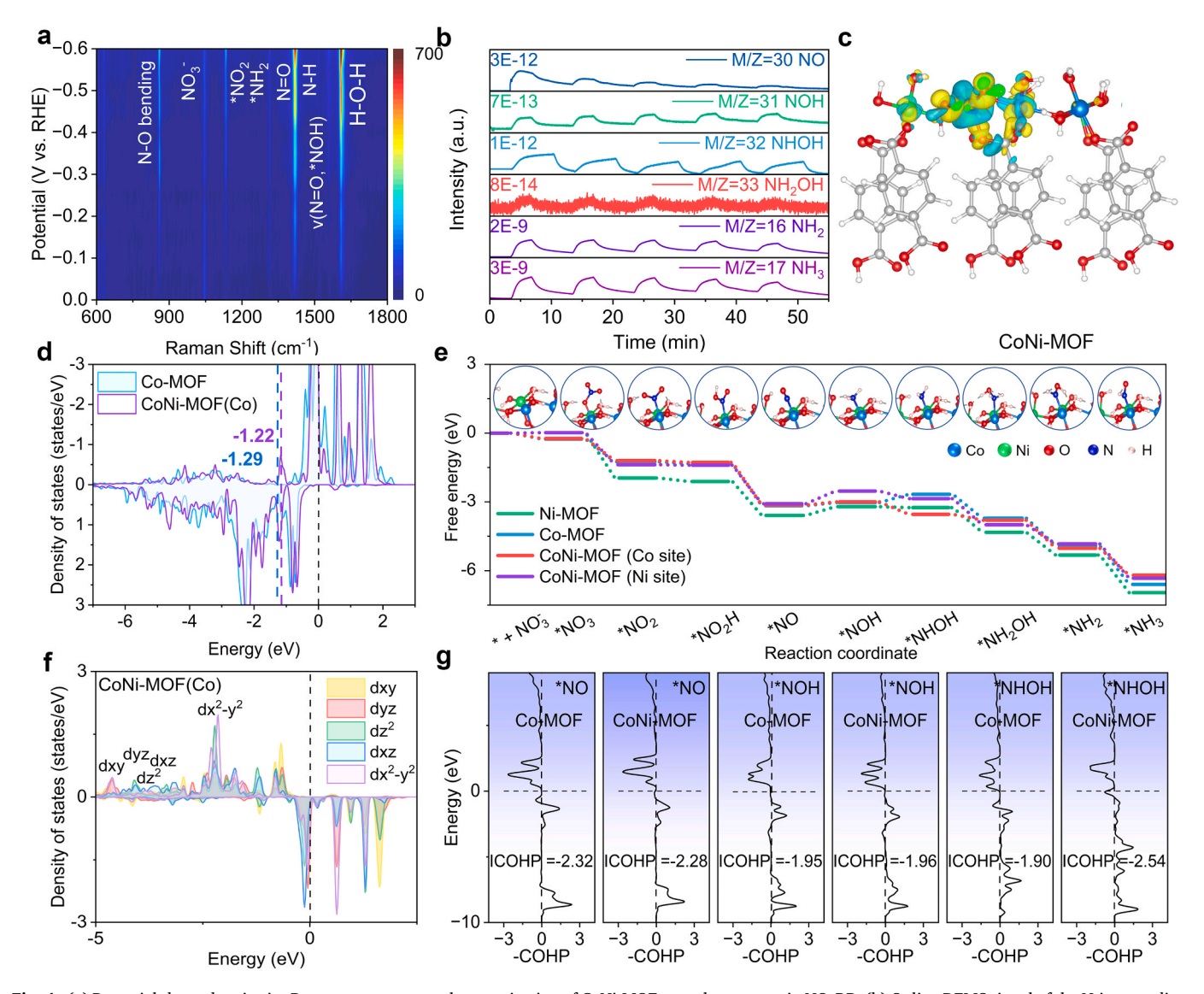


Fig. 4. (a) Potential-dependent in situ Raman spectroscopy characterization of CoNi-MOF nanosheets array in NO_3RR . (b) Online DEMS signal of the N-intermediates in NO_3RR at -0.6 V versus RHE for CoNi-MOF nanosheets array. (c) Differential charge density for Co site in CoNi-MOF. (d) PDOS curves of Co 3d in CoNi-MOF and Co-MOF, and the corresponding d-band center values (ϵ_d , eV). (e) DFT-calculated the free-energy profiles of NO_3RR on CoNi-MOF (Co site), CoNi-MOF (Ni site), Ni-MOF (Ni site), and Co-MOF (Co site), the inset shows the NO_3RR configurations diagram. (f) Projected density of states (PDOS) of Co element in CoNi-MOF. (g) Projected crystal orbital Hamilton populations for the *NO, *NOH and *NHOH intermediates bonded on the Co site over CoNi-MOF and Co-MOF.

To further clarify how the distorted Co-O octahedron affects the catalytic performance, projected density of states (PDOS) of Co element in CoNi-MOF and Co-MOF was acquired. As shown in Fig. 4 f and S36, the position of the five *d*-orbitals of Co for CoNi-MOF was changed upon lattice distortion compared with the normal Co-O octahedron (Co-MOF). Specifically, the energy of d_{z2} moved to the lower energy region, confirming the elongated Co–O bond located along the z-axis [57,58]. In addition, the d_{x2-v2} , d_{xv} , d_{z2} , d_{vz} were more likely to concentrate around the Fermi level, which contributed the up shifted *d*-band center of Co site in CoNi-MOF. And thus, the N-intermediates at Co site delivered an appropriate adsorption strength (Fig. S37). To examine how the redistributed d-orbitals in CoNi-MOF to determine the final catalytic performance, projected crystal orbital Hamiltonian population (COHP) was employed to comprehensively evaluate and investigate the binding capabilities of the respective intermediates before and after lattice distortion in terms of the adsorption and desorption processes. Considering the fluctuation of the energy barrier and endothermic feature for *NO→*NOH→NHOH conversions, the interaction of *NO, *NOH and *NHOH with Co site was investigated. As shown in Fig. 4g, the ICOHP

value for *NO and *NOH on CoNi-MOF(Co site) were –2.28 and –1.96 eV, respectively, comparable with that on Co-MOF, resulting in the similar adsorption energy for *NO and *NOH. In contrast, *NHOH on CoNi-MOF(Co site) delivered a much lower ICOHP value (–2.54 eV) than that on Co-MOF (–1.90 eV), suggesting stronger hybridization ability of N atom of *NHOH with distorted Co site. The weak adsorption energy of *NHOH (–2.67 eV) on the normal Co–O octahedron (Co-MOF) resulted in large energy barrier ($\Delta G_{\rm max}=0.36$ eV) for *NOH \rightarrow NHOH process, making it to be the PDS in NO₃RR. However, the large adsorption energy (–3.54 eV) of *NHOH on CoNi-MOF(Co site) made the *NOH \rightarrow NHOH conversion to be an exothermic process, and the PDS changed to *NO \rightarrow NOH process with lower energy barrier.

3.5. Assembly and performance evaluation of zinc-nitrate batteries

In light of the remarkable NO_3RR performance, CoNi-MOF nanosheets array electrode was further assembled in a zinc-nitrate battery. The battery could integrate the merits of energy output, the removal of nitrates and producing valuable ammonia in one device. As shown in

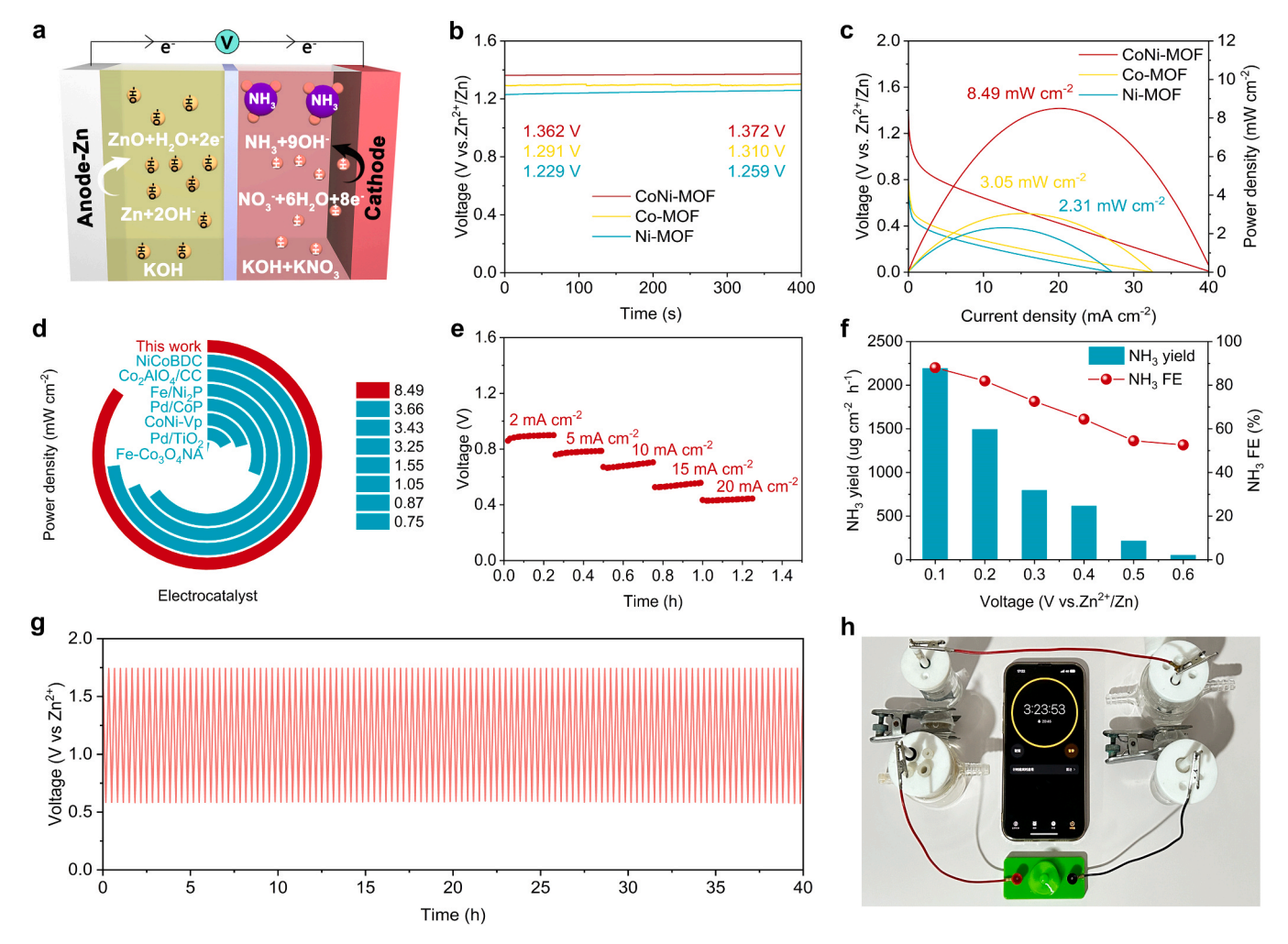


Fig. 5. Schematic diagram of a Zn-NO₃ battery. (b) The open-circuit voltage of Zn-NO₃ cell assembled by CoNi-MOF nanosheets, Co-MOF nanosheets and Ni-MOF nanorods arrays electrodes. (c) Discharge curves and power density of Zn-NO₃ batteries assembled with CoNi-MOF nanosheets, Co-MOF nanosheets and Ni-MOF nanorods arrays cathodes. (d) The comparison of the power density of the CoNi-MOF array electrode with the recently reported cathodes in literature. (e) Discharge voltages at different current densities. (f) Ammonia yield rates and FEs of Zn-NO₃ battery operated at different voltages. (g) Charge-discharge curves of Zn-NO₃ battery at a constant current density of 2 mA cm⁻². (h) Photograph of two connected CoNi-MOF Zn-NO₃ batteries used to power the operation of a small fan.

Fig. 5a, CoNi-MOF nanosheets array electrode was used as the cathode electrode, and a zinc plate served as the anode electrode. The OCV of the battery equipped with CoNi-MOF electrode reached 1.372 V, and remained stable in 400 s, which was higher than that of Ni-MOF (1.259 V) and Co-MOF (1.310 V) based batteries (Fig. 5b). We then tested the discharge curve of the battery, and the corresponding power density was calculated according to the equation of $P = I \times V$ (Fig. 5c). CoNi-MOF array electrode delivered the maximal output power density of 8.49 mW cm⁻², 3.7 and 2.8 times higher than that of the Ni-MOF nanorods (2.31 mW cm⁻²) and Co-MOF nanosheets (3.05 mW cm⁻²) array electrodes, respectively. The enhanced battery performance of the CoNi-MOF array electrode could be attributed to the enhanced nitrate conversion activity. Notably, CoNi-MOF array electrode exceeded the currently reported values in terms of power density both for noble- and non-noble-metal-based cathodes in the literature (Fig. 5d) [59–66].

The rate capability test was further performed by changing the current densities from 2 mA cm $^{-2}$ to 20 mA cm $^{-2}$ (Fig. 5e). The battery displayed a stable discharge plateau, demonstrating the excellent rate capability. To demonstrate the capacity of ammonia production, the zinc-nitrate battery was operated at different discharge voltages (Fig. 5f). At an output voltage of 0.1 V, the maximum ammonia yield reached 2192.2 $\mu g \ cm^{-2} \ h^{-1}$ and a NH $_3$ FE of 88.0 %. The charge-discharge test at a current density of 2 mA cm $^{-2}$ was further carried

out to investigate the stability of the battery (Fig. 5g). Surprisingly, the battery could sustain stable charge-discharge cycles for 40 h, the voltage plateau of the battery stayed steady with no discernible degradation. This suggests the battery has outstanding cycling stability. As shown in Fig. 5h, two connected batteries could power the small fan to run continuously for 3.5 h, demonstrating the excellent application prospects.

4. Conclusions

In summary, an efficient bimetallic CoNi-MOF nanosheets array electrode was constructed for electrochemical nitrate reduction toward ammonia synthesis. The longer Ni–O bonds in linearly arranged CoNi sites effectively compressed the neighboring Co–O octahedron, leading to the stretched distorted Co–O octahedron. The redistributed d-orbital electrons moved up the d-band center of Co site, strengthened the interaction of *NHOH with Co site, and finally transferred the PDS from *NOH→*NHOH to *NO→NOH with much lower energy barrier. Benefitting from the effective regulation of the electronic structure induced by lattice distortion, the synthesized CoNi-MOF delivered enhanced NH $_3$ yield rate of 1.51 mmol cm $^{-2}$ h $^{-1}$ and NH $_3$ FE of 94.1 % at -0.6 V, as well as excellent cycling stability. Additionally, a zinc-nitrate battery was assembled using CoNi-MOF nanosheets array electrode as

the cathode, which delivered a maximum output power density of $8.49~\mathrm{mW~cm^{-2}}$ and an OCV of $1.372~\mathrm{V}$. The battery could power small device to operate stably. This work offers new insight for efficient electrochemical nitrate conversion from the angle of lattice distortion for MOF-base catalysts.

CRediT authorship contribution statement

Shuang Zhao: Conceptualization, Data curation, Formal analysis and Writing – original draft, Validation. Xiaoxuan Chen: Data curation, Software and review. Fan Wu: Conceptualization and Data curation. Junrong Zou: Data curation and Formal analysis. Haiqiao Zhou: Conceptualization and Data curation. Fenglin Xie: Writing – review. Jing Wang: Visualization and Software. Fangfang Wu: Supervision, and Editing. Wei Wang: Supervision and Editing. Peng Gao: Resources, Funding acquisition, Validation, Supervision, and Editing. Weiliu Fan: Visualization, Software and Supervision. Wei Ye: Resources, Funding acquisition, Validation, Supervision, and Editing.

Declaration of Competing Interest

The authors declare that they have no known competing financial interests or personal relationships that could have appeared to influence the work reported in this paper.

Acknowledgements

This work was financially supported in part by the National Natural Science Foundation of China (22479125, 22309039), the University Leading Talents Program of Zhejiang Province (4095C502222140203, 4095C502222140201), the Medical Health Science and Technology Project of the Zhejiang Provincial Health Commission (2023KY1009), We thank Dr. Leijie Zhang (Specreation Instruments Co., Ltd.) for his assistance for XAFS characterization and related data analysis.

Appendix A. Supporting information

Supplementary data associated with this article can be found in the online version at doi:10.1016/j.apcatb.2025.126052.

Data availability

Data will be made available on request.

References

- [1] J.W. Erisman, M.A. Sutton, J. Galloway, Z. Klimont, W. Winiwarter, How a century of ammonia synthesis changed the world, Nat. Geosci. 1 (2008) 636–639.
- [2] G. Qing, R. Ghazfar, S.T. Jackowski, F. Habibzadeh, M.M. Ashtiani, C. Chen, M. R. Smith III, T.W. Hamann, Recent advances and challenges of electrocatalytic N₂ reduction to ammonia, Chem. Rev. 120 (2020) 5437–5516.
- [3] S. Giddey, S. Badwal, C. Munnings, M. Dolan, Ammonia as a renewable energy transportation media, Acs Sustain. Chem. Eng. 5 (2017) 10231–10239.
- [4] S. Li, Y. Zhou, X. Fu, J.B. Pedersen, M. Saccoccio, S.Z. Andersen, K. Enemark-Rasmussen, P.J. Kempen, C.D. Damsgaard, A. Xu, R. Sažinas, J.B.V. Mygind, N. H. Deissler, J. Kibsgaard, P.C.K. Vesborg, J.K. Nørskov, I. Chorkendorff, Long-term continuous ammonia electrosynthesis, Nature 629 (2024) 92–97.
- [5] X. Chen, G. Ren, Y. Wang, Z. Li, Z. Zhang, X. Meng, Introduction of element bi in the P-block promotes N₂ activation for efficient electrocatalytic nitrogen reduction to produce ammonia, Appl. Catal. BEnviron. Energy 355 (2024) 124173.
- [6] B. Li, Y. Zhu, W. Guo, Recent advances of metal oxide catalysts for electrochemical NH₃ production from nitrogen-containing sources, Inorg. Chem. Front. 10 (2023) 5812–5838.
- [7] W. Ye, Y. Yao, X. Wei, M. Xu, S. Zhao, W. Wang, G. Jia, F. Dai, P. Gao, X. Lu, X. Li, B. Xi, N. Wang, S. Xiong, Continuous intermediates spillover boosts electrochemical nitrate conversion to ammonia over dual single-atom alloy, Angew. Chem. Int. Ed. 64 (2025) e202509303.
- [8] Y. Xiong, Y. Wang, J. Zhou, F. Liu, F. Hao, Z. Fan, Electrochemical nitrate reduction: ammonia synthesis and the beyond, Adv. Mater. 36 (2024) 2304021.
- [9] X. Yang, S. Mukherjee, T.O. Carroll, Y. Hou, M.R. Singh, J.A. Gauthier, G. Wu, Achievements, challenges, and perspectives on nitrogen electrochemistry for carbon-neutral energy technologies, Angew. Chem. Int. Ed. 62 (2023) e202215938.

- [10] H. Xu, Y. Ma, J. Chen, W. Zhang, J. Yang, Electrocatalytic reduction of nitrate–a step towards a sustainable nitrogen cycle, Chem. Soc. Rev. 51 (2022) 2710–2758.
- [11] S. Han, H. Li, T. Li, F. Chen, R. Yang, Y. Yu, B. Zhang, Ultralow overpotential nitrate reduction to ammonia via a three-step relay mechanism, Nat. Catal. 6 (2023) 402–414.
- [12] B. Kui, S. Zhao, Y. Hu, K. Zheng, Y. Yao, S. Chen, N. Wang, P. Gao, Z. Bai, W. Ye, Strongly coupled Ag/Cu with MXene for efficient tandem nitrate reduction reaction and zinc–nitrate batteries, Catal. Sci. Technol. 15 (2025) 1617–1626.
- [13] C. Liu, S. Yang, Y. Xiang, L. Wang, Q. Tang, D. Zhu, Electrodeposition of cu on NiCo₂O₄ nanoarrays for efficient electrochemical nitrate reduction to ammonia, Chem. Commun. 61 (2025) 11025–11028.
- [14] C. Wang, Z. Liu, Q. Peng, D. Xing, T. Hu, F. Du, C. Li, R. Ma, H. Yang, C. Guo, Bimetallic Cu₁₁Ag₃ nanotips for ultrahigh yield rate of nitrate-to-ammonium, Angew. Chem. Int. Ed. 64 (2025) e202415259.
- [15] B. Li, P. Xue, M. Qiao, Y. Tang, D. Zhu, Cu doping in FeP enabling efficient electrochemical nitrate reduction to ammonia in neutral media, Chem. Commun. 59 (2023) 13611–13614.
- [16] L. Zhang, Y. Liu, L. Li, T. Wu, Q. Wu, J. Seow, X. Lin, S. Sun, L. Tannesia, Kai Tang, D. Shao, S. Xi, X. Guo, Z.J. Xu, High-efficiency ammonia electrosynthesis from nitrate on ruthenium-induced trivalent cobalt sites, Energy Environ. Sci. 18 (2025) 5622–5631.
- [17] L. Zhang, J. Liang, Y. Wang, T. Mou, Y. Lin, L. Yue, T. Li, Q. Liu, Y. Luo, N. Li, B. Tang, Y. Liu, S. Gao, A. Alshehri, X. Guo, D. Ma, X. Sun, High-performance electrochemical NO reduction into NH₃ by MoS₂ nanosheet, Angew. Chem. 133 (2021) 25467–25472.
- [18] H. Zhang, H. Wang, X. Cao, M. Chen, Y. Liu, Y. Zhou, M. Huang, L. Xia, Y. Wang, T. Li, D. Zheng, Y. Luo, S. Sun, X. Zhao, X. Sun, Unveiling cutting-edge developments in electrocatalytic nitrate-to-ammonia conversion, Adv. Mater. 36 (2024) 2312746.
- [19] L. Liu, L. Zhou, L. Zhang, H. Huang, X. Zhao, Z.J. Xu, Green urea synthesis from CO₂ and nitrogenous small molecules via electrocatalysis and photocatalysis, Small Sci. (2025) 2500289.
- [20] X. Zhang, C. Pei, X. Chang, S. Chen, R. Liu, Z.-J. Zhao, R. Mu, J. Gong, J. Am. Chem. Soc. 142 (2020) 11540–11549.
- [21] Z. Gao, Z.-h Zhao, H. Wang, Y. Bai, X. Zhang, Z. Zhang, H. Mei, M. Yuan, G. Zhang, Jahn-Teller distortions induced by in situ li migration in λ-MnO₂ for boosting electrocatalytic nitrogen fixation. Angew. Chem. Int. Ed. 63 (2024) e202318967.
- [22] B. Zhang, L. Sun, Ru-bda: unique molecular water-oxidation catalysts with distortion induced open site and negatively charged ligands, J. Am. Chem. Soc. 141 (2019) 5565–5580.
- [23] H. Liu, Y. Chen, H. Li, G. Wan, Y. Feng, W. Wang, C. Xiao, G. Zhang, Y. Xie, Construction of asymmetrical dual Jahn–Teller sites for photocatalytic CO₂ reduction, Angew. Chem. Int. Ed. 62 (2023) e202304562.
- [24] K. Mack, A. Wu'nsche von Leupoldt, C. Fo'rster, M. Ezhevskaya, D. Hinderberger, K.W. Klinkhammer, K. Heinze, Effect of chelate ring expansion on Jahn–Teller distortion and Jahn–Teller dynamics in copper (II) complexes, Inorg. Chem. 51 (2012) 7851–7858.
- [25] I.B. Bersuker, Jahn-Teller and pseudo-Jahn-Teller effects: from particular features to general tools in exploring molecular and solid state properties, Chem. Rev. 121 (2021) 1463–1512.
- [26] C. Guan, X. Yue, Y. Liao, Q. Xiang, Structurally asymmetric Ni–O–Mn node in metal–organic layers on carbon nitride support for CO₂ photoreduction, Angew. Chem. Int. Ed. 64 (2025) e202415538.
- [27] G. Kresse, J. Furthmuller, Efficient iterative schemes for ab initio total—energy calculations using a plane—wave basis set, Phys. Rev. B 54 (1996) 11169–11186.
- [28] G. Kresse, J. Hafner, Ab initio molecular dynamics for liquid metals, Phys. Rev. B 47 (1993) 558–561.
- [29] J.P. Perdew, K. Burke, M. Ernzerhof, Generalized gradient approximation made simple, Phys. Rev. Lett. 77 (1996) 3865–3868.
- [30] P.E. Blöchl, Projector augmented—wave method, Phys. Rev. B 50 (1994) 17953–17979.
- [31] S. Grimme, J. Antony, S. Ehrlich, H. Krieg, A consistent and accurate ab initio parametrization of density functional dispersion correction (DFT–D) for the 94 elements H–Pu, J. Chem. Phys. 132 (2010) 154104.
- [32] J.K. Nørskov, J. Rossmeisl, A. Logadottir, L. Lindqvist, J.R. Kitchin, T. Bligaard, H. Jónsson, Origin of the overpotential for oxygen reduction at a fuel—cell cathode, J. Phys. Chem. B 108 (2004) 17886–17892.
- [33] V. Wang, N. Xu, J.-C. Liu, G. Tang, W.-T. Geng, VASPKIT: a user-friendly interface facilitating high-throughput computing and analysis using VASP code, Comput. Phys. Commun. 267 (2021) 108033.
- [34] W. Qiao, I. Waseem, G. Shang, D. Wang, Y. Li, F. Besenbacher, H. Niemantsverdriet, C. Yan, R. Su, Paired electrochemical N-N coupling employing a surface-hydroxylated Ni₃Fe-MOF-OH bifunctional electrocatalyst with enhanced adsorption of nitroarenes and anilines, ACS Catal. 11 (2021) 13510–13518.
- [35] Y. Yao, K. Wei, S. Zhao, H. Zhou, B. Kui, G. Zhu, W. Wang, P. Gao, W. Ye, Highly efficient bifunctional NiFe-MOF array electrode for nitrate reduction to ammonia and oxygen evolution reactions, ACS Sustain. Chem. Eng. 13 (2025) 1245–1252.
- [36] X. Yan, Q.-T. Hu, G. Wang, W.-D. Zhang, J. Liu, T. Li, Z.-G. Gu, NiCo layered double hydroxide/hydroxide nanosheet heterostructures for highly efficient electrooxidation of urea, Int. J. Hydrog. Energy 45 (2020) 19206–19213.
- [37] P.S. Bagus, C.J. Nelin, C.R. Brundle, B.V. Crist, E.S. Ilton, N. Lahiri, K.M. Rosso, Main and satellite features in the ni 2p XPS of NiO, Inorg. Chem. 61 (2022) 18077–18094.

- [38] L. Zhang, T. Liu, N. Chen, Y. Jia, R. Cai, W. Theis, X. Yang, Y. Xia, D. Yang, X. Yao, Scalable and controllable synthesis of atomic metal electrocatalysts assisted by an egg-box in alginate, J. Mater. Chem. A 6 (2018) 18417–18425.
- [39] S. Zhao, Y. Wang, J. Dong, C. He, H. Yin, P. An, K. Zhao, X. Zhang, C. Gao, L. Zhang, J. Lv, J. Wang, J. Zhang, A.M. Khattak, N.A. Khan, Z. Wei, J. Zhang, S. Li, H. Zhao, Z. Tang, Ultrathin metal-organic framework nanosheets for electrocatalytic oxygen evolution, Nat. Energy 1 (2016) 16184.
- [40] W. Gao, Z. Yan, S. Tian, J. Cui, B. Xie, Q. Jiao, C. Zhong, J. Liu, Modulate the strength of *H adsorption by changing the spin state over Cu/Co dual—active sites accelerating ammonia electrochemical synthesis kinetics, Appl. Catal. BEnviron. Energy 377 (2025) 125495.
- [41] K. Zhang, Y. Xu, F. Liu, Q. Wang, X. Zou, M. Tang, M.K.H. Leung, Z. Ao, X. Zhao, X. Zhang, L. An, Leveraging interfacial electric field for smart modulation of electrode surface in nitrate to ammonia conversion, Adv. Sci. 12 (2025) 2410763.
- [42] W. Zhong, Z. Gong, P. Chen, Q. Cao, X. Liu, Y. Chen, Z. Lin, Electrochemical reduction of nitrate to ammonia: from fundamental understanding to practical applications, Chem. Catal. 4 (2024) 101060.
- [43] O.Q. Carvalho, R. Marks, H.K. Nguyen, M.E. Vitale-Sullivan, S.C. Martinez, L. Árnadóttir, K.A. Stoerzinger, Role of electronic structure on nitrate reduction to ammonium: a periodic journey, J. Am. Chem. Soc. 144 (2022) 14809–14818.
- [44] K. Huang, K. Tang, M. Wang, Y. Wang, T. Jiang, M. Wu, Boosting nitrate to ammonia via the optimization of key intermediate processes by low-coordinated Cu–Cu sites, Adv. Funct. Mater. 34 (2024) 2315324.
- [45] B. Zhang, Y. Hou, S. Wang, S. Zhou, Z. Li, Y. Hou, L. Lei, B. Yang, Enhancing universal ph ammonia electrosynthesis kinetics via tandem nanoconfined duallayer catalysis with delayed proton compensation, Appl. Catal. BEnviron. Energy 379 (2025) 125727.
- [46] S. Yu, Y. Zhang, C. Zhang, Y. Zi, Y. Feng, J. Hu, Stability regulation of metal-organic framework materials for electrocatalysis, J. Mater. Chem. A 13 (2025) 4814–4837.
- [47] R. Zhao, Q. Yan, H. Li, T. Yu, X. Yan, Z. Zhu, L. Zhao, J. Liu, Bi-Co corridor construction effectively improving the selectivity of electrocatalytic nitrate reduction toward ammonia by nearly 100%, Adv. Mater. 35 (2023) 2306633.
- [48] J. Park, J. Theerthagiri, N. Yodsin, W. Limphirat, P. Junmon, M. Yong-Choi, CO₂ laser-stabilized Ni-Co dual single-atomic sites for energy generation and ammonia harvesting, Adv. Mater. (2025) 2506137.
- [49] J. Wang, H. Bui, H. Hu, S. Kong, X. Wang, H. Zhu, J. Ma, J. Xu, Y. Liu, L. Liu, W. Chen, H. Bi, M. Yang, F. Huang, T. Brinck, J. Wang, Industrial-current ammonia synthesis by polarized cuprous cyanamide coupled to valorization of glycerol at 4,000 ma cm⁻². Adv. Mater. 37 (2025) 2418451.
- [50] Z. Chang, G. Meng, Y. Chen, C. Chen, S. Han, P. Wu, L. Zhu, H. Tian, F. Kong, M. Wang, X. Cui, J. Shi, Dual-site W-O-CoP catalysts for active and selective nitrate conversion to ammonia in a broad concentration window, Adv. Mater. 35 (2023) 2304508.
- [51] J. Fang, Q. Zheng, Y. Lou, K. Zhao, S. Hu, G. Li, O. Akdim, X. Huang, S. Sun, Ampere-level current density ammonia electrochemical synthesis using CuCo nanosheets simulating nitrite reductase bifunctional nature, Nat. Commun. 13 (2022) 7899
- [52] C. Gong, Y. Peng, M. Xu, X. Wei, G. Sheng, J. Liu, X. Wu, X. Han, F. Dai, J. Dong, Z. Chen, Y. Zhu, W. Ye, Y. Cui, Selective electrocatalytic synthesis of urea using

- entangled iron porphyrins in covalent organic frameworks, Nat. Synth. 4 (2025) 720–729
- [53] K. Yang, S. Han, C. Cheng, C. Guo, T. Li, Y. Yu, Unveiling the reaction mechanism of nitrate reduction to ammonia over cobalt-based electrocatalysts, J. Am. Chem. Soc. 146 (2024) 12976–12983.
- [54] X. Zhao, Y. Jiang, M. Wang, S. Liu, Z. Wang, T. Qian, C. Yan, Optimizing intermediate adsorption via heteroatom ensemble effect over RuFe bimetallic alloy for enhanced nitrate electroreduction to ammonia, Adv. Energy Mater. 13 (2023) 2301409.
- [55] Y. He, Z. Ma, F. Yan, C. Zhu, T. Shen, S. Chou, X. Zhang, Y. Chen, Regulation of the d-band center of metal—organic frameworks for energy-saving hydrogen generation coupled with selective glycerol oxidation, Proc. Natl. Acad. Sci. U. S. A. 121 (2024) e2320777121.
- [56] C. Guan, X. Yue, Q. Xiang, The role of lattice distortion in catalysis: functionality and distinctions from strain, Adv. Mater. 37 (2025) 2501209.
- [57] H. Jia, N. Yao, Z. Liao, L. Wu, J. Zhu, Y. Lao, W. Luo, Understanding the role of spin state in cobalt oxyhydroxides for water oxidation, Angew. Chem. Int. Ed. 63 (2024) e202408005.
- [58] J. Wei, J. Wang, W. Yu, J. Li, Y. Yang, Y. Wang, N. Li, R. Xu, L. Yang, G. Li, P. Dyson, Dual-active-site accelerated hydrogenation facilitates efficient electrochemical reduction of nitrate to ammonia, Appl. Catal. BEnviron. Energy 378 (2025) 125629.
- [59] Z. Deng, J. Liang, Q. Liu, C. Ma, L. Xie, L. Yue, Y. Ren, T. Li, Y. Luo, N. Li, B. Tang, A.A. Alshehri, I. Shakir, P.O. Agboola, S. Yan, B. Zheng, J. Du, Q. Kong, X. Sun, High-efficiency ammonia electrosynthesis on self-supported Co₂AlO₄ nanoarray in neutral media by selective reduction of nitrate, Chem. Eng. J. 435 (2022) 135104.
- [60] Y. Gao, K. Wang, C. Xu, H. Fang, H. Yu, H. Zhang, S. Li, C. Li, F. Huang, Enhanced electrocatalytic nitrate reduction through phosphorus-vacancy-mediated kinetics in heterogeneous bimetallic phosphide hollow nanotube array, Appl. Catal. BEnviron. Energy 330 (2023) 122627.
- [61] R. Zhang, Y. Guo, S. Zhang, D. Chen, Y. Zhao, Z. Huang, L. Ma, P. Li, Q. Yang, G. Liang, C. Zhi, Efficient ammonia electrosynthesis and energy conversion through a Zn-nitrate battery by iron doping engineered nickel phosphide catalyst, Adv. Energy Mater. 12 (2022) 2103872.
- [62] P. Wei, J. Liang, Q. Liu, L. Xie, X. Tong, Y. Ren, T. Li, Y. Luo, N. Li, B. Tang, A. M. Asiri, M.S. Hamdy, Q. Kong, Z. Wang, X. Sun, Iron-doped cobalt oxide nanoarray for efficient electrocatalytic nitrate-to-ammonia conversion, J. Colloid Interface Sci. 615 (2022) 636–642.
- [63] J. Ma, Y. Zhang, B. Wang, Z. Jiang, Q. Zhang, S. Zhuo, Interfacial engineering of bimetallic Ni/Co-MOFs with H-substituted graphdiyne for ammonia electrosynthesis from nitrate, ACS Nano 17 (2023) 6687–6697.
- [64] Y. Gao, K. Wang, S. Li, H. Zhang, F. Huang, Enhancing the selective electrochemical conversion of nitrate via π back-donation on lewis acid sites induced by noble-metal doped CoP, J. Mater. Chem. A 11 (2023) 21161–21169.
- [65] Y. Guo, R. Zhang, S. Zhang, Y. Zhao, Q. Yang, Z. Huang, B. Dong, C. Zhi, Pd doping-weakened intermediate adsorption to promote electrocatalytic nitrate reduction on TiO₂ nanoarrays for ammonia production and energy supply with zinc-nitrate batteries, Energy Environ. Sci. 14 (2021) 3938–3944.
- [66] J. Guan, L. Cai, W. Li, H. Zhou, Y. Huang, Boosting nitrate electroreduction to ammonia on atomic Ru-Co pair sites in hollow spinels, Appl. Catal. BEnviron. Energy 358 (2024) 124387.